Characterization and correction of eddy-current artifacts in unipolar and bipolar diffusion sequences using magnetic field monitoring

Rachel W. Chan [a,*], Constantin von Deuster [b,c], Daniel Giese [c], Christian T. Stoeck [b], Jack Harmer [c], Andrew P. Aitken [c], David Atkinson [a], Sebastian Kozerke [b,c]

[a] Centre for Medical Imaging, University College London, London, United Kingdom
[b] Institute for Biomedical Engineering, University and ETH Zurich, Zurich, Switzerland
[c] Division of Imaging Sciences and Biomedical Engineering, King's College London, London, United Kingdom

ABSTRACT

Diffusion tensor imaging (DTI) of moving organs is gaining increasing attention but robust performance requires sequence modifications and dedicated correction methods to account for system imperfections. In this study, eddy currents in the "unipolar" Stejskal-Tanner and the velocity-compensated "bipolar" spin-echo diffusion sequences were investigated and corrected for using a magnetic field monitoring approach in combination with higher-order image reconstruction. From the field-camera measurements, increased levels of second-order eddy currents were quantified in the unipolar sequence relative to the bipolar diffusion sequence while zeroth and linear orders were found to be similar between both sequences. Second-order image reconstruction based on field-monitoring data resulted in reduced spatial misalignment artifacts and residual displacements of less than 0.43 mm and 0.29 mm (in the unipolar and bipolar sequences, respectively) after second-order eddy-current correction. Results demonstrate the need for second-order correction in unipolar encoding schemes but also show that bipolar sequences benefit from second-order reconstruction to correct for incomplete intrinsic cancellation of eddy-currents.

© 2014 The Authors. Published by Elsevier Inc. This is an open access article under the CC BY license (http://creativecommons.org/licenses/by/3.0/).

1. Introduction

Diffusion-weighted imaging (DWI) and diffusion-tensor imaging (DTI) are non-invasive MRI techniques with broad clinical applications. While many clinical applications of diffusion imaging are in the brain, there is an increasing number of DWI and DTI studies in other organs [1], including the spinal cord [2], breast [3], prostate [4], liver [5], kidney [6], pancreas [7] and in the heart [8,9]. Bulk physiological motion has initially been a barrier to performing diffusion imaging in organs affected by motion. In cardiac diffusion, this has been alleviated by technical advances including the use of cardiac/respiratory navigator techniques, single-shot echo planar imaging (EPI) readouts, and sequence modifications that reduce the effects of any motion that occurs during the diffusion gradients. Such techniques have improved the robustness and reproducibility of diffusion-imaging applications in moving organs such as cardiac DTI [8,9].

Unfortunately, diffusion imaging suffers from substantial artifacts such as those caused by eddy currents, which are induced in conducting structures of the magnet bore by gradient switching. Diffusion imaging is particularly prone to eddy-current artifacts due to relatively long EPI readouts combined with strong diffusion-sensitizing gradients. Unlike static field inhomogeneities, eddy currents do not remain constant over diffusion-encoding directions. Rather, they vary depending upon the magnitude and direction of the applied diffusion gradients. This leads to spatial misregistration and inconsistency between uncorrected images obtained with different diffusion-encoding directions or *b*-values. Ignoring eddy currents in the image reconstruction results in ghosting, bulk object shifts and deformations, as well as signal dropouts [10]. In DTI, this also leads to inaccuracies in estimates of the fractional anisotropy (FA).

In this study, we investigate the effects of eddy currents in sequences that are suitable for performing cardiac DTI where there is substantial motion. Two sequences previously used for cardiac diffusion are compared: (i) the Stejskal-Tanner or "unipolar" spin-echo diffusion sequence [11] and (ii) a "bipolar" spin-echo sequence [12–14]. The unipolar sequence has a shorter echo time

* Corresponding author. Address: Centre for Medical Imaging, 3rd Floor East, 250 Euston Road, London NW1 2PG, United Kingdom.
E-mail address: rachel.chan.ucl@gmail.com (R.W. Chan).

(TE) while the bipolar sequence offers insensitivity to first-order bulk motion through its velocity-compensated nature [12–14].

The twice-refocused sequence, described in Reese et al. [15] (optimized extension of an approach by Wider et al. [16]), was designed to have intrinsic eddy-current compensation. However, this sequence is less suitable for cardiac imaging due to a lack of velocity compensation resulting in a higher likelihood of intravoxel dephasing caused by myocardial motion during the diffusion pulses. Secondly, concomitant gradient fields are unbalanced in the TRSE sequence (whereas they are cancelled out in the bipolar spin-echo sequence due to the symmetry). Lastly, the addition of an extra refocusing pulse makes the sequence more susceptible to RF pulse imperfections. Although adjustments to the gradients and RF pulses can be made to reduce concomitant gradient fields and RF pulse imperfections, the lack of velocity compensation in the TRSE sequence leads to signal loss in the presence of motion. Such signal loss cannot easily be corrected by retrospective methods, and thus, the TRSE sequence is left out of the comparison in this study.

One aim of this study is to investigate the higher-order spatial effects of eddy currents and their time-varying nature [17–21] in the unipolar and bipolar sequences. Correction of higher-order effects have led to improved image quality in previous studies [20–22]. However, the temporal dynamics and relative magnitudes of higher-order effects among different sequences have received less attention. The reason for measuring higher-order effects is that unlike linear offsets, dynamic higher-order phase variations cannot be corrected for by standard pre-emphasis techniques ([23] and references therein).

It is possible to characterize eddy-current induced phase offsets at very high temporal resolution using NMR field probes [24–26]. A dynamic field camera with 16 NMR probes is capable of measuring eddy-current phases up to 3rd spatial order. This technique has recently been used to monitor such phase contributions with first applications to diffusion imaging [20] and phase-contrast imaging [27]. The purpose of the present study is to use a field-monitoring approach to measure, characterize and correct for linear and higher-order eddy-current effects in the unipolar and bipolar sequences. Eddy currents are not patient-specific and the field-monitoring approach potentially allows calibration scans to be used for the correction of temporal and higher-order spatial effects during reconstruction for any organ imaged with a given sequence. As such, this study has been restricted to a phantom study to minimize the confounding effects of additional artifacts, including bulk motion, as found in *in vivo* studies.

2. Methods

2.1. Hardware

All scans were performed on a 3T Philips Achieva TX system (Philips Healthcare, Best, The Netherlands) operated in a gradient mode that provides 63 mT/m maximal strength and 100 mT/m/ ms slew rate. Unipolar and bipolar diffusion sequence diagrams are shown in Fig. 1a and b. A 16-probe dynamic field camera [24–26] (Skope Magnetic Resonance Technologies, Zurich, Switzerland) was used for monitoring the eddy-current fields. Fig. 1c shows a diagram of the field camera. Images were acquired using a phantom and then followed immediately by scans with the field camera.

2.2. Field model

A model of the field was fitted to the signal phases recorded by the 16 ^{1}H NMR probes of the dynamic field camera. The field model used third-order spherical harmonics as described in [24]:

$$\phi(\mathbf{r}, t) = \sum_{l=0}^{N_L-1} k_l(t) h_l(\mathbf{r}) + \omega_{ref}(\mathbf{r}) t \tag{1}$$

where $h_l(\mathbf{r})$ denotes the set of spherical harmonic basis functions for the lth-order real-valued spherical harmonics up to 3rd order with $N_l = 16$ (as in Table 1 of [20]), and $\omega_{ref}(\mathbf{r})$ represents the off-resonance contribution of the imaged object in a reference state at position $\mathbf{r}$. The set of coefficients $\mathbf{k}(t) = [k_0(t), k_1(t), \ldots, k_{N_L-1}(t)]^T$ at time point t was calculated according to:

$$\mathbf{k}(t) = \mathbf{P}^+ [\boldsymbol{\theta}_{probe}(t) - \boldsymbol{\omega}_{ref,probe} t] \tag{2}$$

where $\boldsymbol{\theta}_{probe}(t) = [\theta_1(t), \theta_2(t), \ldots, \theta_{N_P}(t)]^T$ contains phases measured by all N_P probes, $\boldsymbol{\omega}_{ref,probe} = [\omega_{ref,1}, \omega_{ref,2}, \ldots, \omega_{ref,N_P}]^T$ contains the probes' reference frequencies, and $\mathbf{P}^+ = (\mathbf{P}^T \mathbf{P})^{-1} \mathbf{P}^T$ denotes the pseudo-inverse of the so-called probing matrix as in [20],

$$\mathbf{P} = \begin{pmatrix} h_0(\mathbf{r}_1) & h_1(\mathbf{r}_1) & \cdots & h_{N_L-1}(\mathbf{r}_1) \\ \vdots & \vdots & \vdots & \vdots \\ h_0(\mathbf{r}_{N_P}) & h_1(\mathbf{r}_{N_P}) & \cdots & h_{N_L-1}(\mathbf{r}_{N_P}) \end{pmatrix} \tag{3}$$

which samples the basis functions $h_l(\mathbf{r}_\lambda)$ at the probes' locations.

2.3. Image reconstruction

All reconstructions were performed by direct conjugate phase reconstruction in a single step without any iteration. No re-gridding was required. For each coil c, the complex image-space signal at position $\mathbf{r}_\lambda$ and grid index λ reads:

$$\rho_c(\mathbf{r}_\lambda) = \sum_{\kappa}^{N_\kappa} e^{-i\varphi(\mathbf{r}_\lambda, t_\kappa)} d_c(t_\kappa) w(t_\kappa) \tag{4}$$
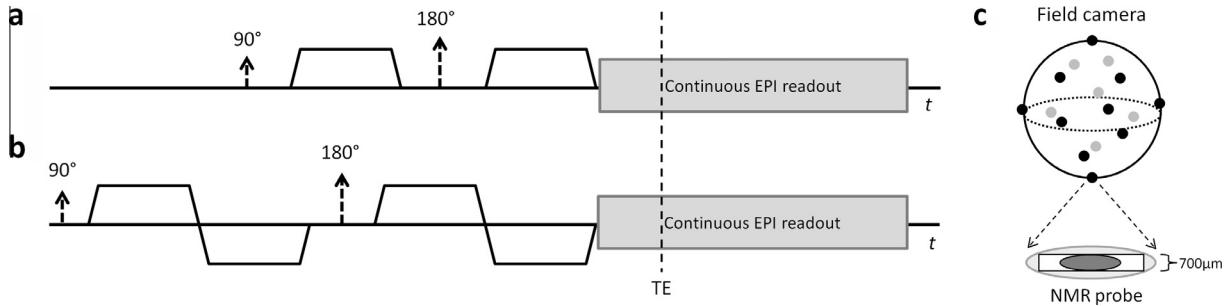
with

$$\varphi(\mathbf{r}_\lambda, t_\kappa) = \sum_{l=0}^{M} k_l(t_\kappa) h_l(\mathbf{r}_\lambda) \tag{5}$$

where d_c is the complex k-space signal for coil c at time t_κ corresponding to sample index κ, φ is the phase measured by the probes, and $w(t_\kappa)$ is the density compensation weights for each k-space sample. Images were reconstructed to a 116×116 matrix size. A standard EPI readout scheme was modified to provide a continuous readout trajectory that consisted of data samples acquired during the ramps of the trapezoidal readout gradients and during the triangular phase-encode blips. Density compensation weights $w(t_\kappa)$ were computed using a 2D Voronoi tessellation approach in k-space [28]. Data from separate channels were combined in image space using a sum-of-squares approach. Parts of the data-processing pipeline were performed using ReconFrame (GyroTools LLC, Zurich, Switzerland).

Images were compared after being reconstructed by the following three methods:

(i) *No eddy-current correction:* Using the set of probe phases $\varphi(\mathbf{r}_\lambda, t_\kappa)$ that were measured during the $b = 0$ s/mm^2 scan, reconstruction was performed using Eqs. (4) and (5) with up to first order (i.e., $M = 3$). The phases from the $b = 0$ s/mm^2 scan provide a nominal trajectory through k-space without the influence of eddy currents due to diffusion gradients. These were used for reconstructing images for all diffusion-encoding directions.

(ii) *Linear eddy-current correction*: Reconstruction included 0th and 1st order phases ($M = 3$) from each diffusion-weighted sequence.

(iii) *Higher-order eddy-current correction*: Reconstruction included 0th to 3rd order phases ($M = 15$).

Fig. 1. Unipolar and bipolar diffusion encoding sequences. DW-EPI spin-echo sequences are shown with (a) unipolar Stejskal-Tanner and (b) bipolar diffusion lobes. Both sequences are sampled with a single-shot EPI readout during which data is continuously acquired and the phase is "monitored" by a separate scan with a field camera. The echo time (TE) is shown by a dotted line during the EPI readout, which corresponds to a partial Fourier factor of 61.2%. (c) A diagram of the field camera is shown. It consists of 16 NMR probes mounted on a sphere having a diameter of 20 cm.

Table 1
Sequence timings.

b-Value	Unipolar		Bipolar	
	TE	Pulse width (ms)	TE	Pulse width (ms)
250	36.3	6.38	53.9	7.51
500	40.3	8.26	60.8	9.28
750	43.0	9.62	66.3	10.63
1000	45.3	10.79	70.2	11.61

Echo times and pulse widths are listed in the table for the unipolar and bipolar sequences for each b-value. Pulse widths for the unipolar sequence are for a single lobe (out of a total of two diffusion lobes that make up the Stejskal-Tanner sequence). Pulse widths for the bipolar sequence are also for a single lobe (out of a total of four diffusion gradient lobes for the bipolar sequence). Pulse widths of each trapezoidal lobe include the ramp up and down times. Ramp durations were 0.9 ms for all gradients. The maximum gradient amplitude per gradient axis was 63 mT/m. The gradients were applied simultaneously on all three gradient axes, which resulted in a maximum resultant gradient amplitude of 87 mT/m.

2.4. MR imaging experiments

An agar phantom was made from an aqueous solution having an agar concentration of 20 g/L mixed with 0.75 g/L of $CuSO_4$. Plastic structures were embedded inside the agar throughout the phantom to probe various spatial locations. Images were obtained using an 8-channel head coil with the following parameters: FOV = 200×155 mm^2, b = [250, 500, 750, and 1000 s/mm^2], minimum TE for each case (TE$_{unipolar}$ = [36.3, 40.3, 43.0, 45.3 ms] and TE$_{bipolar}$ = [53.9, 60.8, 66.3, 70.2 ms] for each b-value respectively), TR = 2 s, 6 diffusion-encoding directions and a b = 0 s/mm^2 image, 1 signal average, 5 mm slice thickness, 61.2% partial Fourier factor, BW$_{PE}$ = 22.4 Hz. The pulse widths of the diffusion lobes (with the corresponding b-values and echo times) are shown in Table 1. A single transverse slice was imaged. The slice was located at the magnet iso-centre. The 180° refocusing pulse was applied orthogonally to the 90° excitation pulse to limit the FOV in the phase-encoding (PE) direction and thereby the EPI readout duration [29]. This would allow the current FOV to be maintained without aliasing if the technique were to be applied in in vivo abdominal scans, where larger FOVs would otherwise be necessary. Diffusion gradients were simultaneously applied on the X, Y and Z gradient axes to achieve higher b-values for a given gradient strength. Second-order shimming was performed using the same shim parameters for all scans.

2.5. Field monitoring

Immediately after the phantom imaging scans, field-monitoring scans were carried out to measure $\theta_{probe}(t)$ using the same diffusion sequences but with the field camera placed inside the scanner

instead of the phantom. For all scans, the full length of the EPI readout was sampled continuously over a duration of 27.1 ms with N_κ = 8192 samples. After subtracting the phases from the b = 0 s/mm^2 scan from those of each diffusion-encoding direction, the phase coefficients $\mathbf{k}(t)$ were obtained. A further set of free-induction decay or "FID scans" were recorded (with and without gradients applied) as in [20,24], to obtain the reference frequencies $\omega_{ref,probe}$ and spatial coordinates of the probes. Scans with the field camera were performed at the same centre frequency as the imaging scans. Any concomitant-field effects that occur during the EPI readout would be implicitly removed by the subtraction of the b = 0 s/mm^2 data as they are present in both diffusion and b = 0 s/mm^2 scans.

2.6. Image analysis

The signal intensity was displayed for intensity profiles along the phase-encoding direction of the image, located at the plastic structures in the phantom (approximately 24 mm from iso-centre) where any misalignments would be visible. Intensity profiles were displayed from each diffusion-encoding direction.

The importance of different orders of correction was assessed by computing displacement maps. For each diffusion-encoding direction δ and at each image location $\mathbf{r}_\lambda$, the phase difference (in radians) between the start and the end of the 27.1 ms readout $\varphi_\delta(\mathbf{r}_\lambda, t_{\kappa=N_\kappa})$ were used. With the approximation that the phase varies linearly over time, a phase ramp was estimated in the PE direction of the EPI readout in k-space, which corresponds to a shift in image space. (Note that the actual phase accrual is non-linear over time, and that the linear approximation is only used to estimate the displacements.) For each diffusion-encoding direction, a pixel-shift map was derived:

$$\Delta y_\delta(\mathbf{r}_\lambda) = \frac{N_y \cdot \varphi_\delta(\mathbf{r}_\lambda, t_{N_y})}{2\pi N_{PE}} \tag{6}$$

where $\Delta y_\delta(\mathbf{r}_\lambda)$ is the number of pixels shifted at pixel index λ, N_y is the reconstructed image matrix size in the PE direction (=116px), N_{PE} is the number of PE lines acquired with partial Fourier (=41). From the pixel-shift maps of each diffusion-encoding direction, the maximum pixel shift was computed by taking the difference between the directions with the maximum and minimum pixel shift, on a pixel-by-pixel basis:

$$\Delta y_{max}(\mathbf{r}_\lambda) = \max_\delta\{\Delta y(\mathbf{r}_\lambda)\} - \min_\delta\{\Delta y(\mathbf{r}_\lambda)\} \tag{7}$$

Maps of the maximum pixel shift were converted into maximum-displacement maps using known voxel sizes. Displacement maps were displayed for the unipolar and bipolar sequences. Displacement maps for the first diffusion direction were also

computed for various eddy-current orders (i.e., up to and including the zeroth, first, second, and third orders) to illustrate the relative contributions of linear and higher-order eddy currents between the two sequences.

The mean fractional anisotropy (FA) and mean diffusivity (MD) were also computed for various levels of eddy-current correction for each sequence. The mean FA and MD were estimated from an ROI placed in the agar phantom, which was assumed to have isotropic diffusion and thus zero FA. Statistical significance was computed using paired t-tests to compare the FA and MD values at various levels of correction.

A standard method of reducing the effects of eddy currents is to perform image registration. Images reconstructed with phase information from the field camera were compared with images corrected using affine image registration. Diffusion tensor images were registered using the FMRIB Software Library (FSL) (http://fsl.fmrib.ox.ac.uk/fsl/fslwiki/FLIRT) [30]. The full FOV of the image was used for registration. Examples of intensity profiles are plotted to visualize differences between registration and eddy-current correction with the field camera.

3. Results

The phase coefficients for each spherical-harmonic order are shown as a function of time in Fig. 2, where the phase deviations arising from unipolar and bipolar diffusion sequences can be compared for the first two diffusion-encoding directions. These curves represent phase contributions from eddy currents alone (since phases of the $b = 0$ s/mm^2 scan have been subtracted). The phases

show distinct evolution patterns that vary between the diffusion-encoding directions, and that differ between unipolar and bipolar sequences. The presence of non-linear temporal components in the phase is evident, particularly in the first orders (Fig. 2c and d). The zeroth, second and third-order phase accumulation varied approximately linearly in time, with only minor deviations. The unipolar case exhibited substantially higher levels of higher-order (i.e., second and third-order) phases (Fig. 2e and g) relative to the bipolar sequence (Fig. 2f and h) for all diffusion-encoding directions (although only the first two directions are shown). The unipolar and bipolar sequences exhibited similar levels of zeroth- and first-order spatial variations. The bipolar sequence was dominated by first-order spatial components (as in Fig. 2d, compared to Fig. 2b and f).

Higher b-values generally led to increased levels of eddy-current phases. Selected phases from different orders (that show greatest phase deviations in the first diffusion-encoding direction) are displayed in Fig. 3, including the z component from the first order, the zy component from the second order and the $5z^3 - 3z(x^2 + y^2 + z^2)$ component of the third order. In the unipolar sequence (Fig. 3a, c, e and g), the amplitude of the phases increased with increasing b-values for every time point in the readout. However, in the bipolar sequence, the first-order curves (Fig. 3d) from different b-values crossed each other during the readout. There were no such crossings in any of the higher-order phases (Fig. 3f and g), where increasing the b-values merely increased the amplitude of the phases throughout the readout.

Fig. 4a shows a $b = 0$ s/mm^2 image of the agar phantom, along with intensity profiles for a single line along the PE direction for
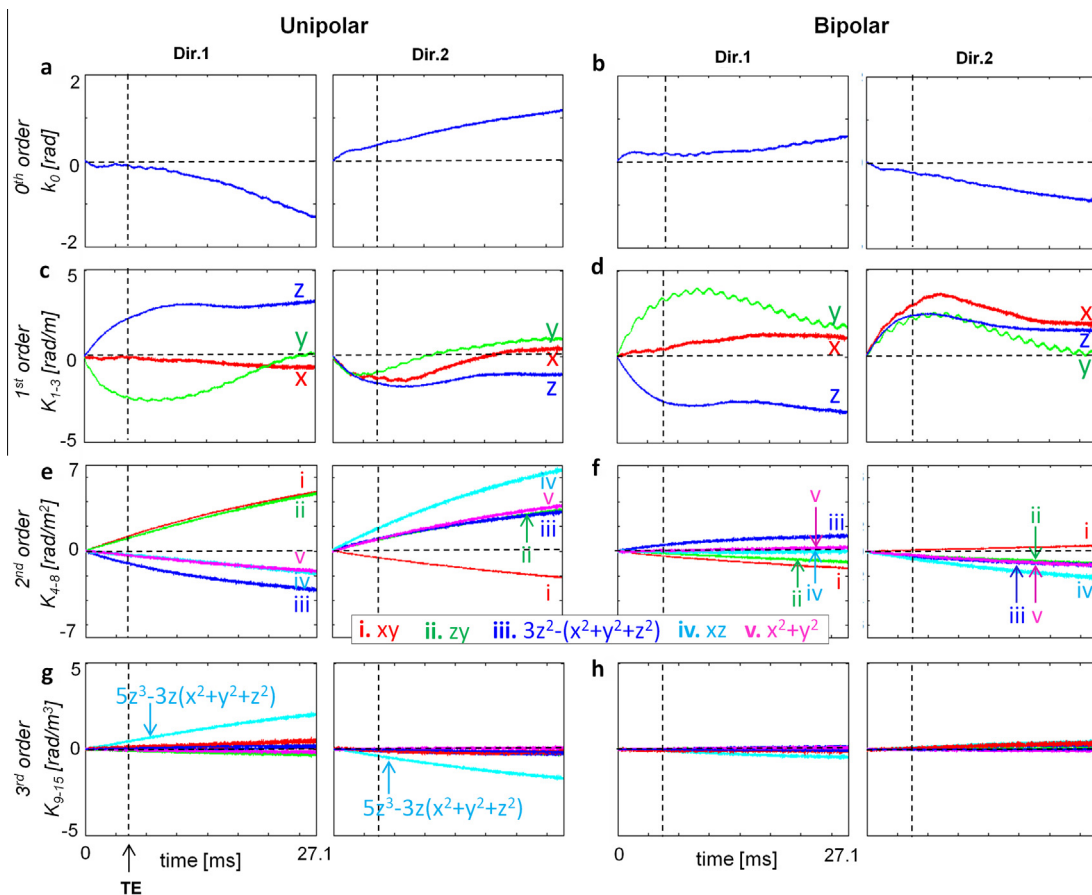
Fig. 2. Phase contributions for different spatial orders. The eddy-current phase coefficients from the $b = 1000$ s/mm^2 scan are shown for various spatial orders: zeroth (a and b), first (c and d), second (e and f), and third orders (g and h) for unipolar and bipolar diffusion schemes. Phase coefficients are shown for the first two diffusion-encoding directions. Phase contributions from the $b = 0$ s/mm^2 image have been subtracted. The echo time is indicated by the dotted vertical line.
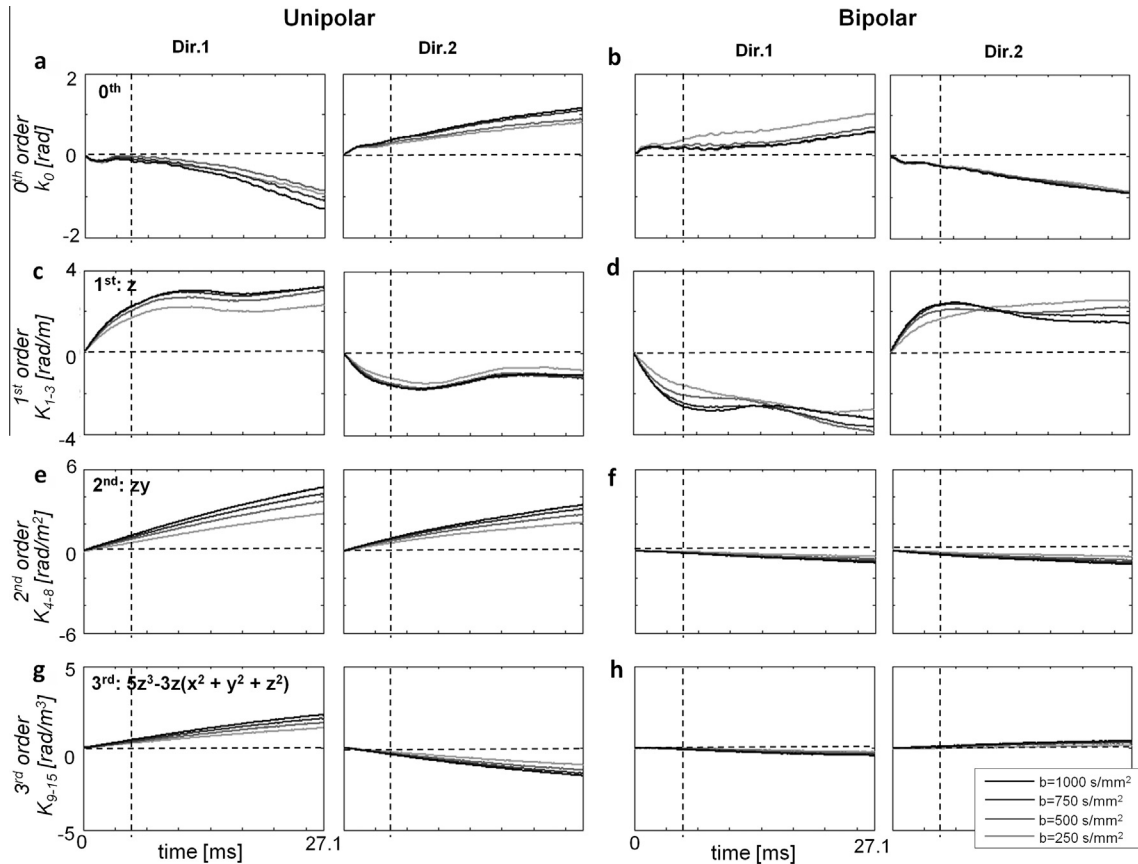
Fig. 3. Phase contributions for multiple b-values. The eddy-current phase coefficients are shown for multiple b-values (250, 500, 750, and 1000 s/mm^2) where higher b-values are displayed in darker grey. Plots show the zeroth-order coefficients (a and b), the z component of the first-order coefficients (c and d), the zy component of the second-order coefficients (e and f) and $5z^3 - 3z(x^2 + y^2 + z^2)$ component of the third-order coefficients (g and h). As in Fig. 2, phase contributions from the $b = 0$ s/mm^2 image have been subtracted. Phase coefficients are shown for the first two diffusion-encoding directions for both unipolar and bipolar schemes. The echo time is indicated by the dotted vertical line.

each of six diffusion directions (Fig. 4b–g) with various orders of eddy-current correction. Fig. 4b and e shows intensity profiles from images that have been reconstructed without eddy-current correction, where image shifts along the phase-encoding direction are evident from misalignment of the plastic structures within the phantom (as indicated by arrows in Fig. 4b and e). The misalignment was more severe in the unipolar sequence. With linear (i.e., zeroth- and first-order) eddy-current correction, the structures were better aligned but residual misalignment was evident in the unipolar case, particularly between the first two diffusion directions (as indicated by the arrow in Fig. 4c). Higher-order (i.e., up to and including third-order) correction reduced the residual misalignment in the unipolar case. For the relatively central profile considered here, linear correction appears to be sufficient in the bipolar sequence to align all the images from different diffusion directions. Although higher-order image reconstruction included both second and third orders, the addition of third orders in the correction resulted in negligible differences in the reconstructed images of the phantom compared to second-order correction in both unipolar and bipolar sequences.

Displacement maps in the image domain are shown for the first diffusion-encoding direction in Fig. 5. Displacements resulting from the zeroth order eddy-current phases (Fig. 5a and e) have spatially-uniform shifts of −0.78 mm for the unipolar sequence and 0.35 mm for the bipolar sequence. The inclusion of first-order components resulted in comparable levels of displacement between the unipolar and bipolar sequences, with maximum displacements of approximately 1 mm for both sequences. Including

displacements from second-order phases (Fig. 5c and g) resulted in displacement levels that were substantially higher in the unipolar sequence (up to approximately 3 mm) compared to that of the bipolar sequence (up to approximately 1.5 mm). Displacement maps that included up to third-order phases (Fig. 5d and h) did not result in any discernible difference compared to those with up to second-order phases (Fig. 5c and g).

Taking into account all diffusion directions (not shown in Fig. 5), the maximum displacements (relative to the $b = 0$ s/mm^2 image) from third-order eddy-currents alone were less than 0.43 mm and 0.29 mm for the unipolar and bipolar sequence, respectively, for the axial plane. Larger contributions were found in the $5z^3 - 3z(x^2 + y^2 + z^2)$ component compared to other third-order components (shown in Fig. 2g). However, third-order displacements of less than 0.96 mm (for the unipolar scheme) and less than 0.31 mm (for the bipolar scheme) were seen in both sagittal and coronal planes.

In Fig. 6a and b, displacement maps are displayed for the unipolar and bipolar sequences, over the six diffusion directions. The maximum displacements in mm (computed for the sum of all eddy-current orders and representing the difference between the maximum positive and negative image shifts over all diffusion-encoding directions) are displayed as contour/colour maps in Fig. 6c and d for the axial plane. Colour maps of the displacements in three orthogonal planes are also shown. The maximum displacements were larger near the edges of the FOV, and showed deviations of up to 6 mm in the unipolar sequence, compared to 2.5 mm in the bipolar sequence. It is important to emphasize that
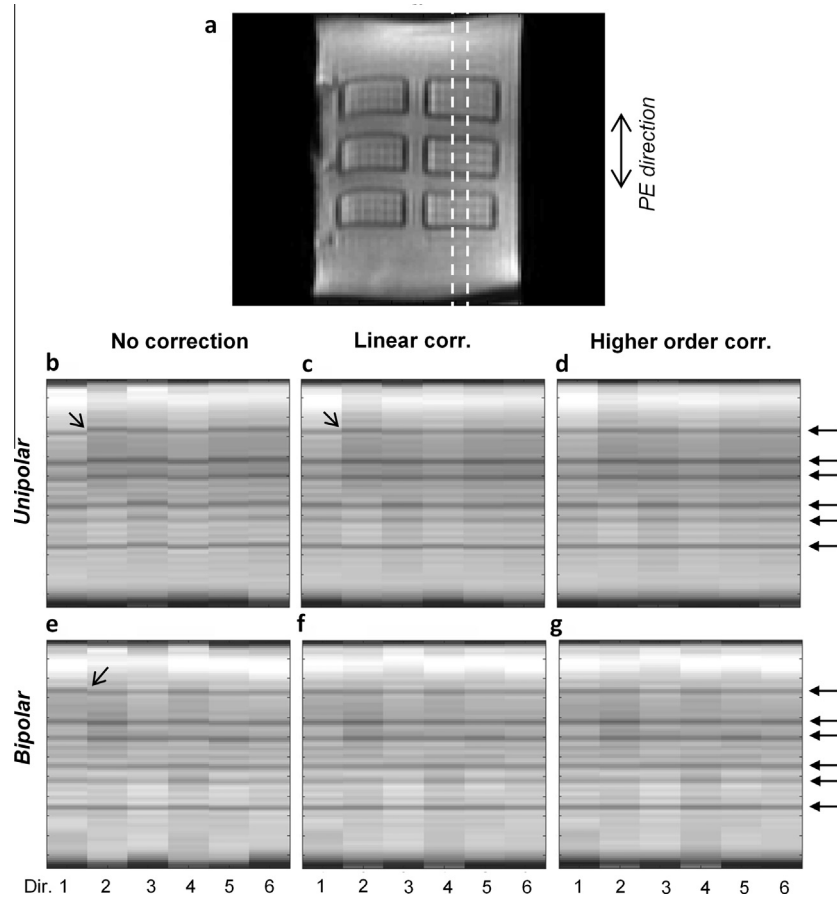
Fig. 4. Phantom images with various levels of eddy-current correction. (a) An image of the agar phantom, acquired with $b = 0$ s/mm^2 and a FOV of 200×155 mm^2, is shown. Cross-section of plastic structures embedded in the agar are seen as rectangular rings that have no signal intensity, in contrast to the agar surrounding (and within) the rings that has higher signal intensity. Five consecutive intensity profiles (between the dotted white lines in figure (a) along the phase-encode direction are averaged to generate averaged intensity profiles. (b–g) Averaged intensity profiles are shown for each diffusion-encoding direction, reconstruction method, and for both unipolar and bipolar schemes, as labelled on the figure. Arrows within figures (b), (c) and (e) point to examples of where structures within the phantom are misaligned between diffusion-encoding directions. Higher-order correction shows alignment of the plastic structures, as in the six horizontal lines of darker intensity, indicated by arrows on the right. Diffusion images were obtained with $b = 1000$ s/mm^2.
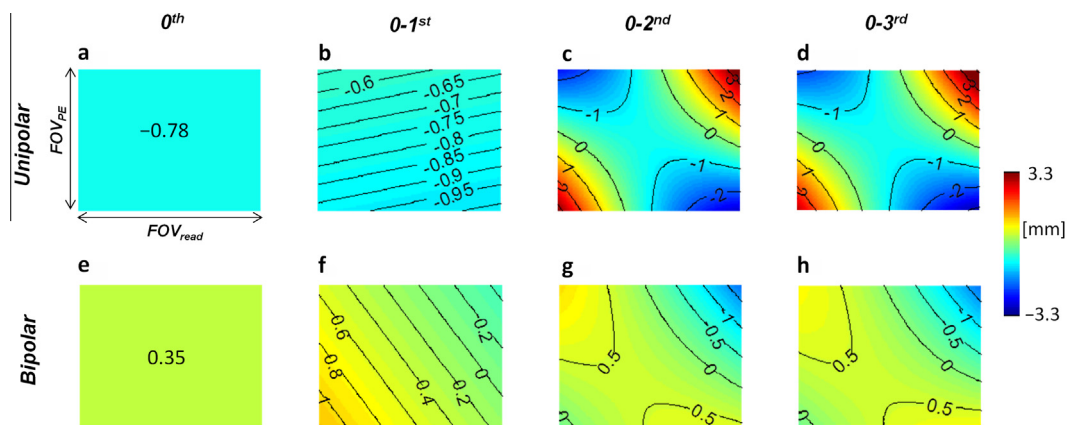

Fig. 5. Displacement maps from different orders of eddy-currents. Displacement maps in the image domain (in mm) are shown for the first diffusion-encoding direction, from eddy-current orders up to and including the (a and e) zeroth order, (b and f) first order, (c and g) second order and (d and h) third order phases. Phase maps are reconstructed to the FOV (200×155 mm^2) and displayed in colour. Eddy-current phases are based on diffusion images acquired with $b = 1000$ s/mm^2. (For interpretation of the references to colour in this figure legend, the reader is referred to the web version of this article.)

the displacements in Figs. 5 and 6 are indicative and calculated using the approximation that the phases have accrued linearly.

In the bipolar sequence, linear correction resulted in significant differences ($p < 0.01$, using paired t-test) in MD compared to the uncorrected case. Linear or higher-order correction resulted in no significant differences in the MD in the unipolar sequence. However, for both unipolar and bipolar sequences, there were significant differences in the FA when linear correction was applied
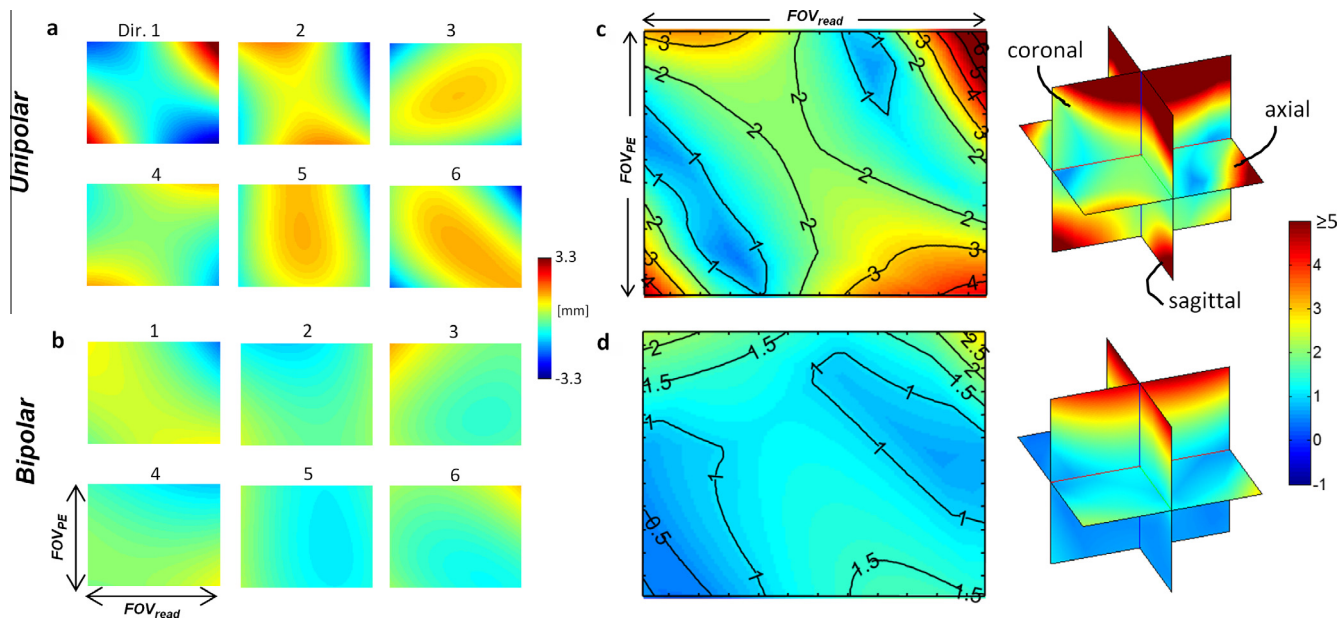
Fig. 6. Displacement maps. (a and b) Estimated displacement maps (in mm) in the image domain are displayed. The image shifts were computed based on the phase evolution at the end of the readout (at 27.1 ms) and include all eddy-current orders. Phase maps are reconstructed to the FOV (200×155 mm^2) and displayed in colour. (c and d) For each pixel, the maximum displacements for all 6 diffusion directions are displayed as a contour/colour map (in the axial plane), for unipolar and bipolar diffusion schemes. Plots of three orthogonal planes are also shown to illustrate displacements for axial, coronal and sagittal planes. Eddy-current phases are based on diffusion images acquired with $b = 1000$ s/mm^2. (For interpretation of the references to colour in this figure legend, the reader is referred to the web version of this article.)

(compared to the uncorrected case, $p < 0.01$ for both sequences), with a marked decrease in the mean FA value with linear correction. No significant differences were seen following higher-order correction (compared to linear correction, $p > 0.01$ for both sequences). However, there was a small decrease in FA with higher-order correction in the unipolar sequences. The mean MD values obtained in the unipolar sequence were 1.945 ± 0.034, 1.945 ± 0.028, and $1.945 \pm 0.027 \times 10^{-3}$ mm^2/s without correction, with linear correction and higher-order correction, respectively. The corresponding MD values of the bipolar sequence were 1.934 ± 0.034, 1.939 ± 0.031, and $1.939 \pm 0.031 \times 10^{-3}$ mm^2/s. The mean FA values from the unipolar scans were 0.050 ± 0.025, 0.042 ± 0.019 and 0.041 ± 0.018 without correction, with linear correction and higher-order correction, respectively. The corresponding FA values from the bipolar sequence were 0.047 ± 0.016, 0.043 ± 0.015 and 0.042 ± 0.015. (Although the standard deviations are relatively large compared to the change in the mean values, the differences in FA between the linear and uncorrected cases prove to be significant.) MD and FA maps (zoomed in over the ROI shown in Fig. 7a) are displayed in Fig. 7b and c, respectively. More uniform MD and FA maps can be seen with higher order correction, especially near the structures where more edge artifacts are visible before eddy-current correction.

In Fig. 8, intensity-profile plots are compared for several image reconstructions. Fig. 8a and b shows the case without image registration or eddy-current correction in the unipolar sequence. Fig. 8c shows the plots after affine image registration where improvements in the alignment can be seen when compared to Fig. 8b. Linear-order eddy-current correction (Fig. 8d) performed better than affine image registration (Fig. 8c). Higher-order eddy-current correction (Fig. 8e) resulted in small differences in the signal intensity compared to linear-order eddy-current correction (Fig. 8d).

4. Discussion

In both unipolar and bipolar sequences, the phases exhibited non-linear spatial and temporal behaviour. This suggests that it is important to measure higher spatial orders by using adequate numbers of field probes and to capture time-varying effects with sufficient temporal resolution. In particular, non-linear time-varying effects were found in the spatially-linear eddy-current phases.

Higher levels of second-order eddy currents were found in the unipolar sequence compared to the bipolar sequence. The bipolar diffusion sequence was dominated by linear orders. Although the bipolar sequence suffers from lower SNR relative to the unipolar sequence (due to longer echo times for the same b-value), advantages of the bipolar sequence are that it is velocity-compensated and that it is less susceptible to the effects of second-order eddy currents. However, second-order image reconstruction remains beneficial for the bipolar sequence where image displacements were reduced from approximately 1.5 mm to 0.29 mm with second-order correction. One of the third-order components, $5z^3 - 3z(x^2 + y^2 + z^2)$, had an increased amplitude relative to the other third-order eddy-current contributions. However, maximum displacements from third-order eddy currents were less than 0.96 mm. If the displacements from third-order eddy currents can be considered negligible, then 9 NMR probes would be sufficient in these sequences for measuring up to second-order eddy-current phases at high temporal resolution.

In Fig. 3, crossings during the readout were seen in the linear-order phases in the bipolar sequence. This is characteristic of phase contributions from incomplete cancellation of eddy-currents or inaccurate pre-emphasis. Complex phase behaviour with increasing b-values was seen in the bipolar case while the unipolar sequence lacked such crossings. This sequence difference is possibly related to the fact that there were more gradient switches in the diffusion-sensitizing gradients of the bipolar sequence, with eddy-currents arising from more time-points. The specific timing of gradient switches depended on the b-value. Eddy currents cancel each other if a gradient switch is closely followed in time by an opposite gradient switch [17,31–33]. However, the switching of strong gradients with relatively long temporal separation (as in diffusion imaging) results in incomplete cancellation and residual eddy currents.
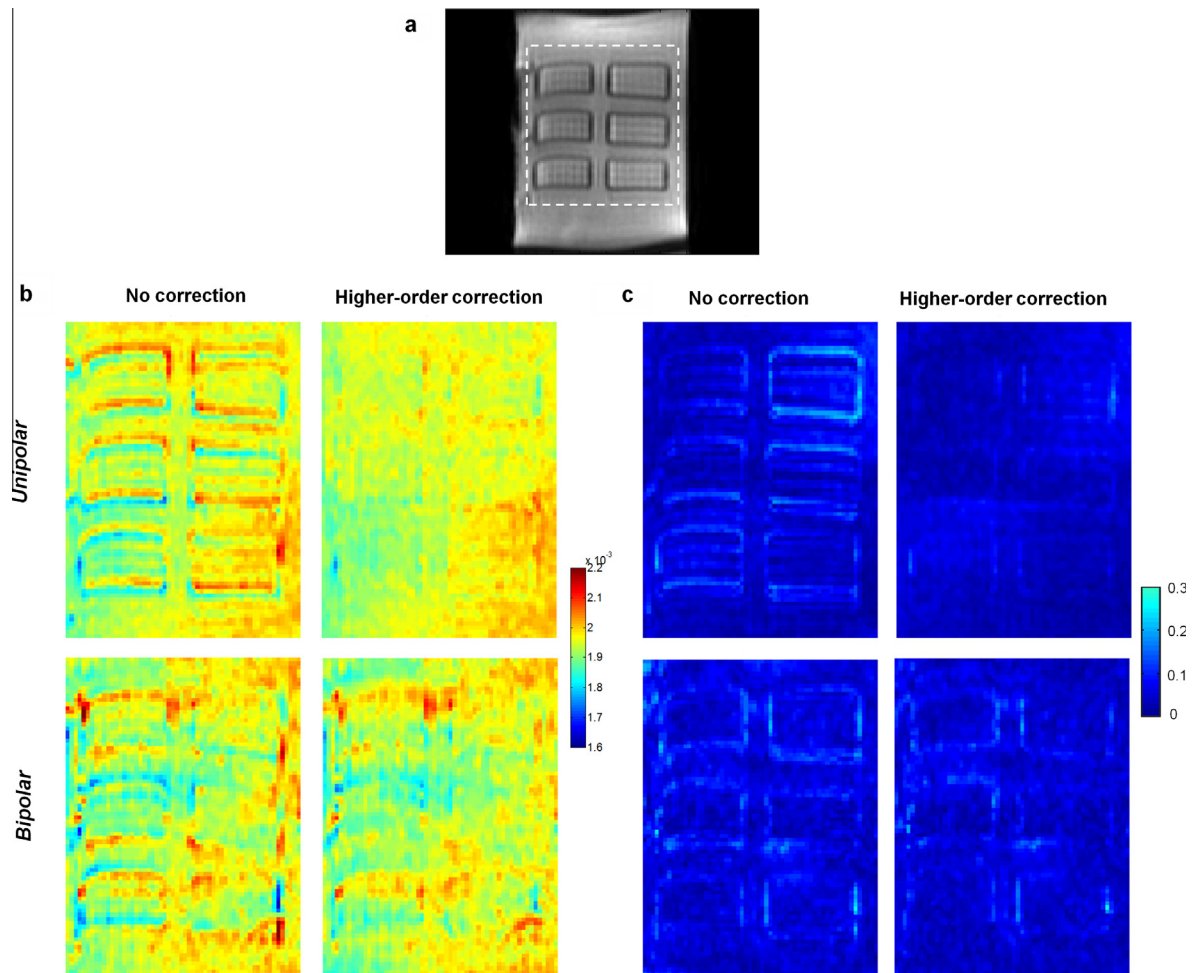
Fig. 7. Fractional anisotropy (FA) and mean diffusivity (MD) at various levels of eddy-current correction. (a) A region of interest is shown by the dotted white line over the relevant structures of the phantom, for display of MD and FA maps. (b) MD maps with and without higher order correction. (c) FA maps with and without higher order correction.

The linear accumulation of 0th-order phases could be related to a drift in the centre frequency between the calibration and phantom scans. The second- and third-order phases had relatively linear accrual that persisted beyond the readout. This suggests the presence of eddy currents with relatively long time constants. Compared to those with intermediate time constants, eddy-currents with longer time constants have better self-cancellation properties (following opposite gradient switches of trapezoidal diffusion pulses). However, neither will completely cancel out since the gradient switches are not coincident in time. The field camera is sensitive to small residual eddy-current phases resulting from incomplete cancellation [20,34,35].

The gradient pre-emphasis was on and its effects were included in the measured phases. Thus, any residual eddy currents contribute to the shape of the observed phases. More comprehensive models are required to fully describe eddy-current behaviour [34,35]. The gradient impulse response method is free from model restrictions and can measure residual eddy-currents phases that do not conform to those predicted by simple models with limited sets of exponential terms. In general, the specific shapes of the eddy-current phases can only be predicted closely by characterizing the entire frequency behaviour of the gradient system [34,35].

In a clinical setting, the TE would be determined by the maximum b-value in the set. The other (lower) b-values in the set would have lower gradient amplitudes and thus, less eddy current

distortions. However, the purpose in this study was to measure the maximum eddy-current contribution (by applying the diffusion pulses at maximum gradient strength with shortest TE) to determine the worst case scenario at each chosen b-value.

Decreases in FA with linear-order eddy-current correction were consistent with expectations given an isotropic phantom with an assumed FA value of zero. A further decrease in FA was seen with higher-order correction in the unipolar sequence, since there were more substantial higher-order eddy currents in the unipolar sequence relative to the bipolar sequence. The MD was found to be more robust against eddy-currents compared to the FA in this isotropic phantom, since higher-order correction did not result in significant changes in the MD in either the unipolar or bipolar sequence. Differing MD values between bipolar and unipolar sequences could have been because they were estimated at different TEs and result in different SNRs. In a truly isotropic phantom where FA is zero, noise results in an upward bias in the FA and a negative bias in the MD (due to an apparently insufficient decay in the diffusion signal). In addition to noise, the positive bias in the measured FA could also have been caused by systemic errors including the calibration of the diffusion gradients, the possibility that the phantom did not truly have an FA of zero, or by the presence of mechanical motion. Although the same b-values were used for comparison between the unipolar and bipolar sequence, different waveforms resulting in different diffusion times could also
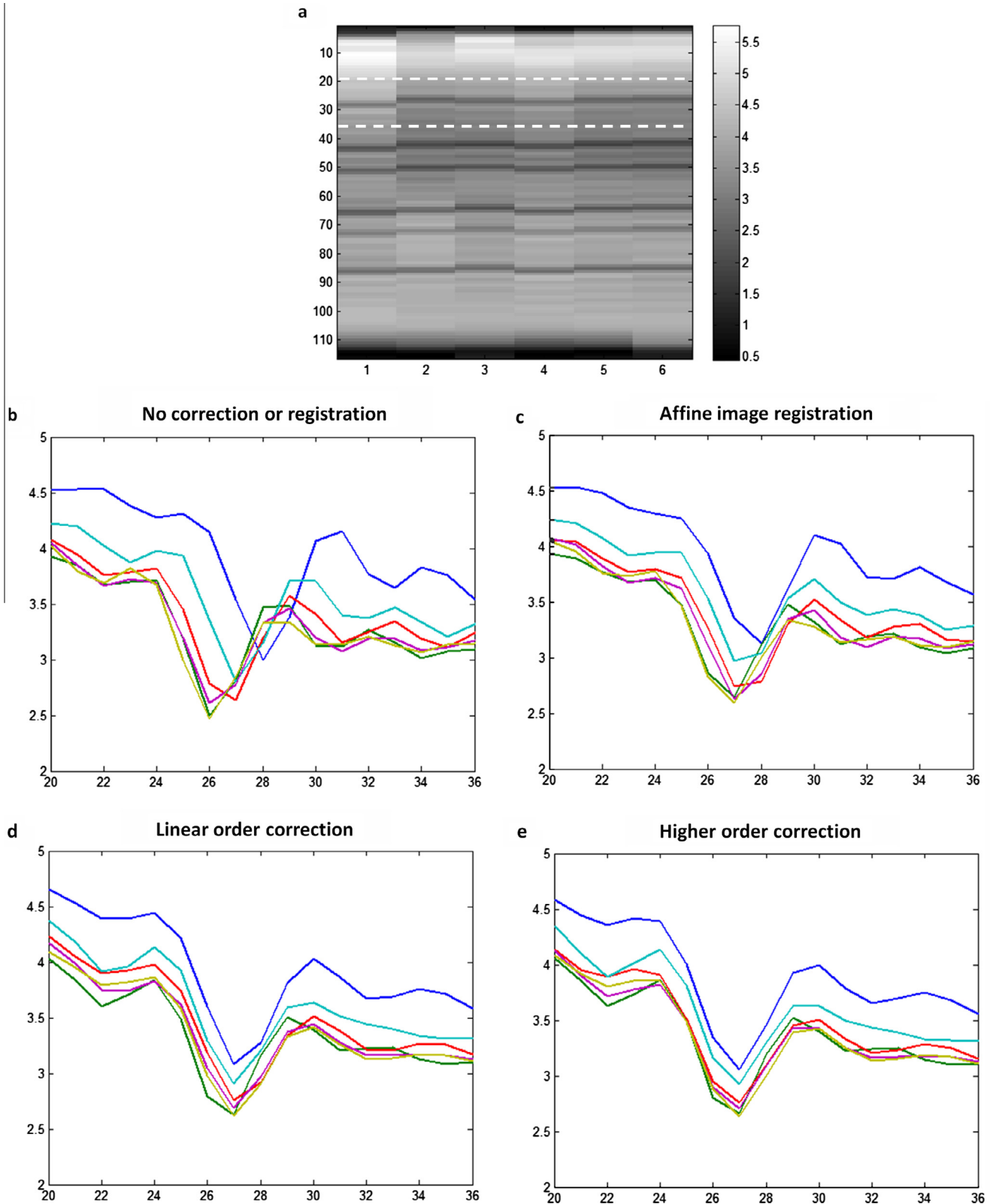
Fig. 8. Comparison between registration and eddy-current correction. Intensity profiles for six diffusion-encoding directions in (b)–(e) are plotted for a relevant section of the image shown within the dotted lines in (a), for the unipolar sequence with a b-value of 1000 s/mm². (a) The image of intensity profiles is shown for the unregistered, uncorrected case. Intensity plots are shown (b) without registration or eddy-current correction, (c) after affine image registration, (d) after linear-order eddy-current correction, and (e) higher-order eddy-current correction including third orders.

have led to a different q-values, and hence, signal intensity. The use of minimum TEs in this study reflects how the sequences would be used in clinical practice.

Comparison of eddy-current corrected images with affine image registration shows that eddy-current correction with phases from the field camera performs better than image registration. In the

presence of higher-order eddy-current distortions, it was expected that affine image registration would leave residual misalignment artifacts. The ability to correct distortions with image registration will depend on the anatomy of interest and the nature of the eddy-current distortions. The drawback of affine image registration is that even if the distortions can be aligned, the intensities may not be fully recovered. Image registration has been shown to be suboptimal for diffusion images that have significant contrast changes due to directional anisotropy [36,37]. Another disadvantage of image registration is SNR dependency. It was found that image registration performed better on diffusion images obtained at lower *b*-values than those at higher *b*-values where the SNR was low [38]. Eddy-current correction with the field camera is expected to perform well regardless of the SNR in the image. However, the drawback of eddy-current correction with the field camera is that extra hardware is required.

It was found that performing the first step of the full iterative procedure (as described in Wilm et al. [20]), i.e., conjugate phase reconstruction, was adequate for removing bulk object shifts arising from higher-order terms. Conjugate-phase correction without iterative methods was sufficient because the field variations were slowly-varying [39]. In general, iterative methods would be necessary [20] and faster methods [40] have been developed to speed up the reconstruction process.

Only a single transverse slice was imaged in the phantom, which was unaffected by eddy-current components that vary in the *z*-direction. However, it is expected that correction would work well for all orientations since the eddy-current phases were measured in three dimensions on a sphere. With the NMR probes located at a fixed radius on a sphere, the volume over which the correction can be performed can be extended outside the radius of the field camera unless there are spatial non-linearities in the gradients. The non-uniformity of the field produced by gradient coils was not taken into account for the determination of the probe locations. Gradients were assumed to be linear within the 20 cm diameter of the field camera.

Oscillations were seen in some phase coefficients, particularly the *y* gradient, which could be due to mechanical resonances [34,41] or possibly related to the EPI readout [20]. Mechanical vibrations could be the cause of the residual signal variation between different diffusion-encoding directions seen in Fig. 4. Another possible cause for this signal variation could be the eddy currents from the first diffusion lobe affecting the 180° refocusing pulse. Incomplete refocusing can result in non-linear effects across the image, which would be different for each diffusion-encoding direction. Correcting for incomplete refocusing would require measurement of eddy-current phases during the refocusing pulse, as well as subsequent correction of unwanted phase contributions in the slice-refocusing gradients for every diffusion-encoding direction.

The addition of parallel imaging can be used to reduce the readout train length and hence the level of distortions. However, in this study, the temporal eddy-current phases showed accumulation early in the readout, suggesting that eddy-current correction may offer improvements even for the short readouts enabled by parallel imaging. Reducing the FOV by the use of orthogonal excitation and refocusing pulses is an alternative approach for reducing distortion levels. Similar distortion levels can be maintained, for example, by using a parallel-imaging reduction factor of two with a doubled FOV and the same readout length. Although parallel imaging enables larger FOVs without increasing the level of distortions, the reduced-FOV method (by orthogonal excitation pulses) remains useful for imaging smaller FOVs where parallel imaging can be less effective due to the lack of coil-sensitivity variation over these smaller FOVs. In this study, the reduced-FOV method was used to effectively minimize the readout length, and hence, the level of distortions before eddy-current correction. Although the current reduced-FOV approach only allowed a single slice to be acquired, alternative reduced FOV methods have been demonstrated for imaging multiple contiguous slices. This includes tilted excitation methods [42,43] and a method where additional refocusing pulses are applied for recovering the magnetization after the orthogonal excitation and refocusing pulses [44].

Future work in eddy-current correction would benefit from improvements that have been made to field-camera technology to allow continuous monitoring of the phases using a time-interleaved approach [45], which would allow monitoring of the phases during the diffusion-encoding pulse itself. It is also possible to compute the impulse-response function by deconvolution methods [34,35]. The gradient impulse-response function could be computed once and applied to any gradient waveform including the diffusion-encoding gradients. In addition, concurrent field-monitoring can be achieved with fluorine-based field probes [46,47], which would allow simultaneous acquisition of the imaging data and measurement of field offsets for eddy-current correction.

5. Conclusions

The use of a field camera is a valuable approach for characterizing the time-varying nature of eddy currents of higher spatial orders. This study has demonstrated that there are higher levels of second- and third-order eddy-currents in the unipolar spin-echo diffusion sequence compared to the bipolar diffusion sequence. Second-order eddy-current correction results in improved image quality and reduced misalignment artifacts, particularly for the unipolar diffusion sequence. In choosing between the unipolar and bipolar sequences for performing diffusion imaging in the presence of bulk motion, both the echo time and the level of higher-order eddy-current contributions should be considered. The unipolar sequence offers shorter echo times, while the bipolar sequence, as well as being velocity-compensated, offers the advantage of reduced higher-order eddy currents.

References

[1] C. Schmid-Tannwald, A. Oto, M.F. Reiser, C.J. Zech, Diffusion-weighted MRI of the abdomen: current value in clinical routine, J. Magn. Reson. Imag. 37 (1) (2013) 35–47, http://dx.doi.org/10.1002/jmri.23643.

[2] J.B. Andre, R. Bammer, Advanced diffusion-weighted magnetic resonance imaging techniques of the human spinal cord, Top. Magn. Reson. Imag. 21 (6) (2010) 367–378, http://dx.doi.org/10.1097/RMR.0b013e31823e65a1.

[3] F.P. Pereira, G. Martins, V. Carvalhaes de Oliveira Rde, Diffusion magnetic resonance imaging of the breast, Magn. Reson. Imag. Clin. N. Am. 19 (1) (2011) 95–110, http://dx.doi.org/10.1016/j.mric.2010.09.001.

[4] S. Sinha, U. Sinha, In vivo diffusion tensor imaging of the human prostate, Magn. Reson. Med. 52 (2004) 530–537, http://dx.doi.org/10.1002/mrm.20190.

[5] H. Chandarana, B. Taouli, Diffusion and perfusion imaging of the liver, Eur. J. Radiol. 76 (3) (2010) 348–358, http://dx.doi.org/10.1016/j.ejrad.2010.03.016.

[6] M. Notohamiprodjo, M.F. Reiser, S.P. Sourbron, Diffusion and perfusion of the kidney, Eur. J. Radiol. 76 (3) (2010) 337–347, http://dx.doi.org/10.1016/j.ejrad.2010.05.033.

[7] N.C. Balci, W.H. Perman, S. Saglam, F. Akisik, R. Fattahi, M. Bilgin, Diffusion-weighted magnetic resonance imaging of the pancreas, Top. Magn. Reson. Imag. 20 (1) (2009) 43–47, http://dx.doi.org/10.1097/RMR.0b013e3181b48667.

[8] S. Nielles-Vallespin, C. Mekkaoui, P. Gatehouse, T.G. Reese, J. Keegan, P.F. Ferreira, S. Collins, P. Speier, T. Feiweier, R. de Silva, M.P. Jackowski, D.J. Pennell, D.E. Sosnovik, D. Firmin, In vivo diffusion tensor MRI of the human heart: reproducibility of breath-hold and navigator-based approaches, Magn. Reson. Med. 70 (2013) 454–465, http://dx.doi.org/10.1002/mrm.24488.

[9] N. Toussaint, C.T. Stoeck, T. Schaeffter, S. Kozerke, M. Sermesant, P.G. Batchelor, In vivo human cardiac fibre architecture estimation using shape-based diffusion tensor processing, Med. Image Anal. 17 (8) (2013) 1243–1255, http://dx.doi.org/10.1016/j.media.2013.02.008.

[10] P. Jezzard, A.S. Barnett, C. Pierpaoli, Characterization of and correction for eddy current artifacts in echo planar diffusion imaging, Magn. Reson. Med. 39 (5) (1998) 801–812.

[11] E.O. Stejskal, J.E. Tanner, Spin diffusion measurements: spin echoes in the presence of a time-dependent field gradient, J. Chem. Phys. 42 (1) (1965) 288–292.

[12] U. Gamper, P. Boesiger, S. Kozerke, Diffusion imaging of the in vivo heart using spin echoes-considerations on bulk motion sensitivity, Magn. Reson. Med. 57 (2) (2007) 331–337.

[13] C.T. Stoeck, N. Toussaint, P. Boesiger, P.G. Batchelor, S. Kozerke, Sequence timing optimization in multi-slice diffusion tensor imaging of the beating heart, in: Proceedings of the 19th Annual Meeting of ISMRM, Montreal, Quebec, Canada, 2011, p. 282.

[14] M. Ozaki, Y. Inoue, T. Miyati, H. Hata, S. Mizukami, S. Komi, K. Matsunaga, R. Woodhams, Motion artifact reduction of diffusion-weighted MRI of the liver: use of velocity-compensated diffusion gradients combined with tetrahedral gradients, J. Magn. Reson. Imag. 37 (1) (2013) 172–178, http://dx.doi.org/10.1002/jmri.23796.

[15] T.G. Reese, O. Heid, R.M. Weisskoff, V.J. Wedeen, Reduction of eddy-current-induced distortion in diffusion MRI using a twice-refocused spin echo, Magn. Reson. Med. 49 (1) (2003) 177–182.

[16] G. Wider, V. Dotsch, K. Wuthrich, Self-compensating pulsed magnetic-field gradients for short recovery times, J. Magn. Reson. Ser. A 108 (2) (1994) 255–258.

[17] C. Boesch, R. Gruetter, E. Martin, Temporal and spatial analysis of fields generated by eddy currents in superconducting magnets: optimization of corrections and quantitative characterization of magnet/gradient systems, Magn. Reson. Med. 20 (2) (1991) 268–284.

[18] J.J. Vanvaals, A.H. Bergman, Optimization of eddy-current compensation, J. Magn. Reson. 90 (1) (1990) 52–70.

[19] K. Edler, D. Hoult, Spherical harmonic inductive detection coils for dynamic pre-emphasis, Magn. Reson. Med. 60 (2) (2008) 277–287, http://dx.doi.org/10.1002/mrm.21693.

[20] B.J. Wilm, C. Barmet, M. Pavan, K.P. Pruessmann, Higher order reconstruction for MRI in the presence of spatiotemporal field perturbations, Magn. Reson. Med. 65 (6) (2011) 1690–1701, http://dx.doi.org/10.1002/mrm.22767.

[21] D. Xu, J.K. Maier, K.F. King, B.D. Collick, G. Wu, R.D. Peters, R.S. Hinks, Prospective and retrospective high order eddy current mitigation for diffusion weighted echo planar imaging, Magn. Reson. Med. 70 (2013) 1293–1305, http://dx.doi.org/10.1002/mrm.24589.

[22] Y. Shen, D.J. Larkman, S. Counsell, I.M. Pu, D. Edwards, J.V. Hajnal, Correction of high-order eddy current induced geometric distortion in diffusion-weighted echo-planar images, Magn. Reson. Med. 52 (2004) 1184–1189.

[23] N.G. Papadakis, K.M. Martin, J.D. Pickard, L.D. Hall, T.A. Carpenter, C.L. Huang, Gradient preemphasis calibration in diffusion-weighted echo-planar imaging, Magn. Reson. Med. 44 (4) (2000) 616–624.

[24] C. Barmet, N. De Zanche, B.J. Wilm, K.P. Pruessmann, A transmit/receive system for magnetic field monitoring of in vivo MRI, Magn. Reson. Med. 62 (1) (2009) 269–276, http://dx.doi.org/10.1002/mrm.21996.

[25] C. Barmet, B.J. Wilm, M. Pavan, K.P. Pruessmann, A third-order field camera with microsecond resolution for MR system diagnostics, in: Proceedings of the 17th Annual Meeting of ISMRM, Honolulu, Hawaii, USA, 2009, p. 781.

[26] N. De Zanche, C. Barmet, J.A. Nordmeyer-Massner, K.P. Pruessmann, NMR probes for measuring magnetic fields and field dynamics in MR systems, Magn. Reson. Med. 60 (1) (2008) 176–186, http://dx.doi.org/10.1002/mrm.21624.

[27] D. Giese, M. Haeberlin, C. Barmet, K.P. Pruessmann, T. Schaeffter, S. Kozerke, Analysis and correction of background velocity offsets in phase-contrast flow measurements using magnetic field monitoring, Magn. Reson. Med. 67 (5) (2012) 1294–1302, http://dx.doi.org/10.1002/mrm.23111.

[28] V. Rasche, R. Proska, R. Sinkus, P. Börnert, H. Eggers, Resampling of data between arbitrary grids using convolution interpolation, IEEE Trans. Med. Imag. 18 (1999) 385.

[29] D.A. Feinberg, J.C. Hoenninger, L.E. Crooks, L. Kaufman, J.C. Watts, M. Arakawa, Inner volume MR imaging: technical concepts and their application, Radiology 156 (3) (1985) 743–747.

[30] M. Jenkinson, S. Smith, A global optimisation method for robust affine registration of brain images, Med. Image Anal. 5 (2) (2001) 143–156.

[31] A.L. Alexander, J.S. Tsuruda, D.L. Parker, Elimination of eddy current artifacts in diffusion-weighted echo-planar images: the use of bipolar gradients, Magn. Reson. Med. 38 (6) (1997) 1016–1021.

[32] R.F. Fischer, C. Barmet, M. Rudin, P. Boesiger, K.P. Pruessmann, S. Kozerke, Monitoring and compensating phase imperfections in cine balanced steady-state free precession. Magn. Reson. Med., 2013. http://dx.doi.org/10.1002/mrm.24606 (in press).

[33] J. Finsterbusch, Double-spin-echo diffusion weighting with a modified eddy current adjustment, Magn. Reson. Imag. 28 (3) (2010) 434–440, http://dx.doi.org/10.1016/j.mri.2009.12.004.

[34] S.J. Vannesjo, M. Haeberlin, L. Kasper, M. Pavan, B.J. Wilm, C. Barmet, K.P. Pruessmann, Gradient system characterization by impulse response measurements with a dynamic field camera, Magn. Reson. Med. 69 (2013) 583–593, http://dx.doi.org/10.1002/mrm.24263.

[35] S.J. Vannesjo, B.E. Dietrich, M. Pavan, D.O. Brunner, B.J. Wilm, C. Barmet, K.P. Pruessmann, Field camera measurements of gradient and shim impulse responses using frequency sweeps. Magn. Reson. Med., 2013. http://dx.doi.org/10.1002/mrm.24934 (in press).

[36] G.K. Rohde, A.S. Barnett, P.J. Basser, S. Marenco, C. Pierpaoli, Comprehensive approach for correction of motion and distortion in diffusion-weighted MRI, Magn. Reson. Med. 51 (2004) 103–114, http://dx.doi.org/10.1002/mrm.10677.

[37] M.E. Bastin, Correction of eddy current-induced artifacts in diffusion tensor imaging using iterative cross-correlation, Magn. Reson. Imag. 17 (1999) 1011–1024.

[38] K. O'Brien, A. Daducci, N. Kickler, F. Lazeyras, R. Gruetter, T. Feiweier, G. Krueger, 3-D residual eddy current field characterisation: applied to diffusion weighted magnetic resonance imaging, IEEE Trans. Med. Imag. 32 (8) (2013) 1515–1525, http://dx.doi.org/10.1109/TMI.2013.2259249 (06.05.13) Epub.

[39] H. Eggers, T. Knopp, D. Potts, Field inhomogeneity correction based on gridding reconstruction for magnetic resonance imaging, IEEE Trans. Med. Imag. 26 (3) (2007) 374–384.

[40] B.J. Wilm, C. Barmet, K.P. Pruessmann, Fast higher-order MR image reconstruction using singular-vector separation, IEEE Trans. Med. Imag. 31 (7) (2012) 1396–1403, http://dx.doi.org/10.1109/TMI.2012.2190991.

[41] D. Gallichan, J. Scholz, A. Bartsch, T.E. Behrens, M.D. Robson, K.L. Miller, Addressing a systematic vibration artifact in diffusion-weighted MRI, Hum. Brain Mapp. 31 (2) (2010) 193–202, http://dx.doi.org/10.1002/hbm.20856.

[42] C.A. Wheeler-Kingshott, S.J. Hickman, G.J. Parker, O. Ciccarelli, M.R. Symms, D.H. Miller, G.J. Barker, Investigating cervical spinal cord structure using axial diffusion tensor imaging, Neuroimage 16 (2002) 93–102.

[43] B.J. Wilm, J. Svensson, A. Henning, K.P. Pruessmann, P. Boesiger, S.S. Kollias, Reduced field-of-view MRI using outer volume suppression for spinal cord diffusion imaging, Magn. Reson. Med. 57 (3) (2007) 625–630.

[44] E.K. Jeong, S.E. Kim, J. Guo, E.G. Kholmovski, D.L. Parker, High-resolution DTI with 2D interleaved multislice reduced FOV single-shot diffusion-weighted EPI (2D ss-rFOV-DWEPI), Magn. Reson. Med. 54 (2005) 1575–1579.

[45] B.E. Dietrich, C. Barmet, D. Brunner, K.P. Pruessmann, An Autonomous System for Continuous Field Monitoring with Interleaved Probe Sets, ISMRM 2011, Montreal, Canada, ID: 1842, 2011.

[46] C. Barmet, B.J. Wilm, M. Pavan, G. Katsikatsos, J. Keupp, G. Mens, K.P. Pruessmann, Concurrent higher-order field monitoring for routine head MRI: an integrated heteronuclear setup, in: Proceedings of the 18th Annual Meeting of ISMRM, Stockholm, Sweden, 2010, p. 216.

[47] B.J. Wilm, C. Barmet, C. Reischauer, K.P. Pruessmann, Concurrent higher-order field monitoring eliminates thermal drifts in parallel DWI, in: Proceedings of the 18th Annual Meeting of ISMRM, Stockholm, Sweden, 2010, p. 781.